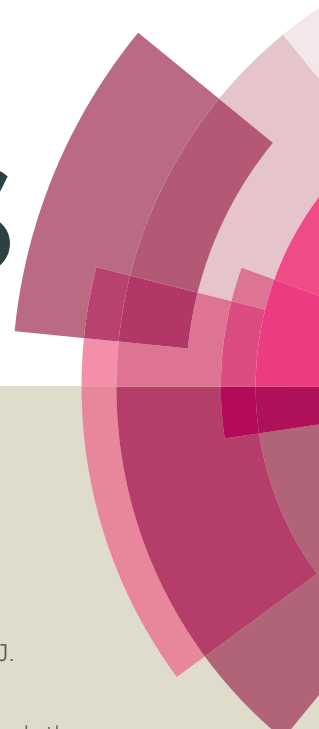


RSC Advances



This article can be cited before page numbers have been issued, to do this please use: Y. Chen, W. Li, J. Wang, Q. Yang, Q. Hou and M. Ju, *RSC Adv.*, 2016, DOI: 10.1039/C6RA11390G.



This is an *Accepted Manuscript*, which has been through the Royal Society of Chemistry peer review process and has been accepted for publication.

Accepted Manuscripts are published online shortly after acceptance, before technical editing, formatting and proof reading. Using this free service, authors can make their results available to the community, in citable form, before we publish the edited article. This *Accepted Manuscript* will be replaced by the edited, formatted and paginated article as soon as this is available.

You can find more information about *Accepted Manuscripts* in the [Information for Authors](#).

Please note that technical editing may introduce minor changes to the text and/or graphics, which may alter content. The journal's standard [Terms & Conditions](#) and the [Ethical guidelines](#) still apply. In no event shall the Royal Society of Chemistry be held responsible for any errors or omissions in this *Accepted Manuscript* or any consequences arising from the use of any information it contains.

Gold nanoparticles-modified TiO₂/SBA-15 nanocomposites as active plasmonic photocatalysts for the selective oxidation of aromatic alcohols

Yu Chen, Weizun Li, Jingyu Wang, Qian Yang, Qidong Hou, Meiting Ju*

College of Environmental Science and Engineering, Nankai University, Tianjin 300071, China

Abstract

The catalytic performance of noble-metal nanocatalysts on mesoporous silica hosts has been widely investigated because the effects of localized surface plasmon resonance (LSPR) can open new avenues for the improvement of catalytic performance under light irradiation. In this study, a series of photoactive Au/TiO₂/SBA-15 catalysts were developed for the selective oxidation of alcohols to corresponding aldehydes and ketones. The catalysts thus developed were characterized by X-ray diffraction (XRD), Brunauer–Emmett–Teller (BET) analysis, transmission electron microscopy (TEM), high-angle annular dark-field scanning transmission electron microscopy (HAADF-STEM), scanning transmission electron microscopy energy-dispersive spectrometry, X-ray photoelectron spectroscopy (XPS), transient photocurrent response and electrochemical impedance spectroscopy (EIS). Au and small TiO₂ nanoparticles (NPs) were uniformly anchored into the SBA-15 channels by the microwave-assisted alcohol reduction, resulting in the increase of the interfacial area between gold and titania; this increase in turn results in better catalytic performance for the Au₂/TiO₂/SBA-15 catalysts toward the selective oxidation of aromatic alcohols to aromatic aldehydes (ketones) as a result of the efficient pore confinement and visible-light absorption by the LSPR effect. A scheme with respect to the enhancement of photooxidation induced by the LSPR effect on the Au NP-decorated TiO₂/SBA-15 composite was proposed.

Keywords: Photocatalysis; Gold nanoparticles; Porous materials; Aromatic alcohols; Selective oxidation

* Corresponding author. Tel.: +86 022-23500589
Email: jumeit@nankai.edu.cn (M. Ju)

Introduction

In organic synthesis, the selective oxidation of alcohols to corresponding carbonyl compounds (such as aldehydes or ketones) is a crucial reaction because carbonyl compounds are valuable as both intermediates as well as high-value components in the perfume, confectionery, and pharmaceutical industries¹⁻⁶. Typically, aldehydes and ketones are oxidized using stoichiometric amounts of oxidizing agents, such as chromate or permanganate; however, these reagents are toxic and not cost-effective⁷. From an environmental viewpoint, it is of significance to develop methods involving the use of molecular oxygen as the primary oxidant in the presence of a catalyst.

The photocatalytic selective oxidation of alcohols by semiconductor materials such as titanium dioxide (TiO₂) with molecule oxygen (O₂) as an oxidant at room temperature has been proposed as an attractive, environmentally benign method for organic synthesis⁸⁻¹⁴. Several types of substrates, such as alcohols, amines, hydrocarbons, and sulfides, are successfully oxidized at atmospheric pressure and room temperature¹⁵⁻¹⁷. However, one of the typical drawbacks for the practical application of photocatalytic processes includes poor visible-light harvesting and low quantum efficiencies under visible-light irradiation, which is the main component of solar irradiation. Recently, plasmonic metal nanoparticles (NPs) have demonstrated promise for harvesting photon energy for chemical reactions, attributed to their extraordinary and tailorable localized surface plasmon resonance (LSPR) properties¹⁸⁻²¹. Upon light irradiation, plasmonic metal nanoparticles supported on semiconductors produce *hot electrons* (e⁻) via the intraband transition of 6sp band electrons, which are injected into the semiconductor, resulting in direct charge separation on the plasmonic NPs. In this manner, plasmonic NPs can transfer solar energy to neighboring semiconductors or molecular complexes for driving chemical reactions.

This scenario has motivated the advantage of the plasmonic effect for aerobic oxidation. Tsukamoto et al.²² have reported the aerobic oxidation of benzylic alcohols with TiO₂-loaded Au particles at room temperature under visible-light irradiation ($\lambda > 420$ nm) and found that the location of Au NPs is crucial for the promotion of electron transfer from LSPR-excited Au NPs to TiO₂. The Au NPs, with a diameter of less than 5 nm, located at the interface between anatase and

rutile TiO_2 particles behave as the active sites for the photoreaction, affording high yields of aldehyde or ketone products in toluene under visible-light irradiation. Schünemann et al.²³ have reported a remarkably small bimetallic AuCu nanoparticles with diameter of 2 nm supported on ordered mesoporous silica (SBA-15, KIT-6, and MCM-41) and highly selective (90%) for the oxidation of glycerol to dihydroxyacetone. They also found that the small gold–copper bimetal NPs are sufficiently large to permit the absorption of visible light by LSPR while simultaneously providing a large catalytically active surface area, contributing to high activity. Typically, the catalytic properties of Au strongly depend on its particle size and active surface area²⁴. Considering the previous pioneering studies, ordered mesoporous materials such as MCM-41 and SBA-15 with multiple channel structures and high surface areas have emerged as one of the most promising candidates, in which Au NPs can be anchored in channels; hence, the diameter of Au NPs can be sufficiently large to permit visible-light absorption by LSPR and to provide a large catalytically active surface area.

These previous studies have enlightened us to design and synthesize gold-nanoparticle-modified $\text{TiO}_2/\text{SBA-15}$ nanocomposites as active plasmonic photocatalysts, where Au NPs are sufficiently large to permit visible-light absorption by LSPR while simultaneously providing a catalytically large active surface area. Herein, we report the preparation of a series of $\text{Au}/\text{TiO}_2/\text{SBA-15}$ composite photocatalysts with varying contents of gold in the range from 0.5 wt% to 5 wt%. The photocatalytic selective aerobic oxidation of alcohols at ambient temperature was performed under visible-light irradiation for evaluating the characteristics of $\text{Au}/\text{TiO}_2/\text{SBA-15}$ based on its nanoscale architectures. The effects of precursor concentration and synthetic process on the gold particle size and light absorption were characterized by sophisticated techniques, such as XRD, HRTEM, HAADF-STEM, FESEM, XPS, nitrogen adsorption, Fourier transform-IR, UV–vis absorption spectroscopy, transient photocurrent response and electrochemical impedance spectroscopy. Interdependent interactions between the loading and size of gold particles and support material were investigated in detail. The dependence of the photocatalytic oxidation of benzyl alcohol on wavelength was also discussed. Based on the results, the photocatalytic selective aerobic oxidation of alcohols over $\text{Au}/\text{TiO}_2/\text{SBA-15}$ under visible-light irradiation in the photocatalytic process was proposed.

Experimental section

The Au/TiO₂/SBA-15 composites were synthesized by two-step microwave assisted hydrothermal reaction approach, which can be seen in our previous works²⁵. A typical procedure was as follows: SBA-15 (1.0 g) and was sonicated in 20 mL ethanol for 2 h, and then, tetrabutyl orthotitanate (2.0 g) was added dropwise with stirring for 1 h. Next, the homogeneous solution was transferred into a 100 mL Teflon-lined autoclave, which was then placed in a microwave-hydrothermal synthesis system (MDS-6, Sineo, Shanghai, China) and maintained at 180°C for 30 min. After the hydrothermal reaction, the resulting composite was collected and washed with distilled water, followed by rinsing in ethanol, and then dried in an oven at 80°C, for 24 h, in air. The TiO₂/SBA-15 was dried under reduced pressure at 120°C to remove absorbed water. The dried powder (0.5g) and a desired amount of H₂AuCl₄ solution (10 mg/ml) was quickly injected into system. The mixed solution was placed under reduced pressure to incorporate the Au precursor into the mesopores of TiO₂/SBA-15 by capillary forces. The suspension were irradiated by microwave under an Ar atmosphere for 5min. After filtration and washing with ethanol and distilled water, the resulting powder was dried at 80 °C overnight under air. A series of Au supported TiO₂/SBA-15 labeled as Au_x/TiO₂/SBA-15 (Au wt.% = 0.5, 1.0, 2.0, 5.0 respectively) with different amount of Au were obtained by the adding desired amount of H₂AuCl₄ solution in the reaction system. For reference, the Au supported by P25 TiO₂ nanoparticles and SBA-15 were also prepared using the same method and Au/TiO₂/SBA-15 sample with similar Au loading (~2.0%) was prepared through photodeposition method, which was denoted as Au/TiO₂/SBA-15-PD.

To identify the TiO₂ and gold phases, X-Ray diffraction (XRD) measurements were performed using a PANalytical X'pert MRD with a step size of 0.02° in the region of 2θ=10-80°. Diffuse reflectance UV-Vis spectra of the samples (ca.20 mg diluted in ca. 80 mg of BaSO₄) were recorded in the air against BaSO₄ in the region of 200 to 800 nm on a Shimadzu 3600 UV-Vis spectrophotometer. The morphologies of the TiO₂ composites were measured by scanning electron microscopy (SEM) on a Hitachi S-4800 microscope. Transmission electron microscopy (TEM) and high angle annular dark field detector (HAADF) images were recorded using an FEI Tecnai G2-F20 microscope at an accelerating voltage of 200 kV. Energy-dispersive X-ray (EDX) and

EDX elemental mapping were performed on Oxford-Instruments X-MaxN to visualize the elemental compositions of the products. X-ray photoelectron spectra (XPS) of the samples were recorded on a Thermo Fisher Scientific ESCALAB 250XI using a monochromated Al-Ka X-ray source. The specific surface areas were determined through N₂ adsorption/desorption isotherms collected at -196°C on a TriStar II 3020 adsorption analyzer. The samples were degassed under vacuum at 200°C for 4 hours prior to analysis. The FTIR spectra were recorded on Nicolet IS50 spectrophotometer equipped with a diamond attenuated total reflectance (ATR) smart accessory. The samples for IR were prepared by mixing the catalysts (100 mg) and benzyl alcohol (1 mL) together for 4 h in the dark at room temperature, followed by drying the specimens at 80°C for 24 h. The samples were held in glass surface dishes and no washing was performed after adsorbing benzyl alcohol. The spectrum of pure benzyl alcohol was also collected for comparison. The photocurrent measurement and electrochemical impedance spectroscopy (EIS) measurement, were carried out in a standard three electrode cell containing 0.5 mol L⁻¹ Na₂SO₄ aqueous solution with a platinum foil and a saturated calomel electrode as the counter electrode and the reference electrode, respectively, on a CHI 760D workstation (Shanghai, China). A 300 W Xe lamp with a 420 nm cutoff filter was chosen as a visible light source. All of the electrochemical measurements were performed at room temperature.

Photocatalytic selective oxidation of alcohols was performed in a 15-mL a home-made reactor sealed with rubber stoppers. Typically, 50 mg of Au/TiO₂/SBA-15 was spread into the reactor, then 5 mL of toluene (solvent) and 50 μmol of alcohol (reactant) were injected into the reactor. The bottle was filled with molecular oxygen for 5 min and sealed with a rubber septum cap. Then, the bottle was ultrasonicated at room temperature for 5 min to distribute the catalyst evenly in the solution. The reactor was photoirradiated under magnetic stirring using a 300 W xenon lamp (PLS-SXE 300, Beijing Perfectlight, Co. Ltd.) filtered through a glass filter to provide light with wavelengths $\lambda > 420$ nm. The reaction temperature was controlled at room temperature by a water-cooling system. Control photoactivity experiments using different radical scavengers (ammonium oxalate (AO) as a scavenger for photogenerated holes, tert-butyl alcohol as a scavenger for hydroxyl radicals, AgNO₃ as a scavenger for electrons, and benzoquinone as a scavenger for superoxide radical species) were performed similar to the above photocatalytic oxidation of alcohols except that radical scavengers (50 μmol) were added to the reaction system.

After the reactions, the organic products were analyzed by a GC (Thermo Fisher TRACE 1310GC) equipped with a flame ionization detector. GC-MS analysis using a Thermo Fisher TRACE ISQ GCMS, equipped with a TR-50MS capillary column (Thermo Fisher, 30 m×0.320 mm×0.25μm), was used for product identification. The column oven temperature was programmed from 40°C (held for 1min) to 280°C at a rate of 20°C min⁻¹. The catalyst was recovered by carefully washed with anhydrous ethanol and deionized water and dried in an oven at 80°C overnight for the following cycling photoactivity test. The conversion of alcohol and yield of aldehyde were defined as follows:

$$\text{Conversion (\%)} = [(C_0 - C_{\text{alcohol}})/C_0] \times 100$$

$$\text{Yield (\%)} = C_{\text{aldehyde}}/C_0 \times 100$$

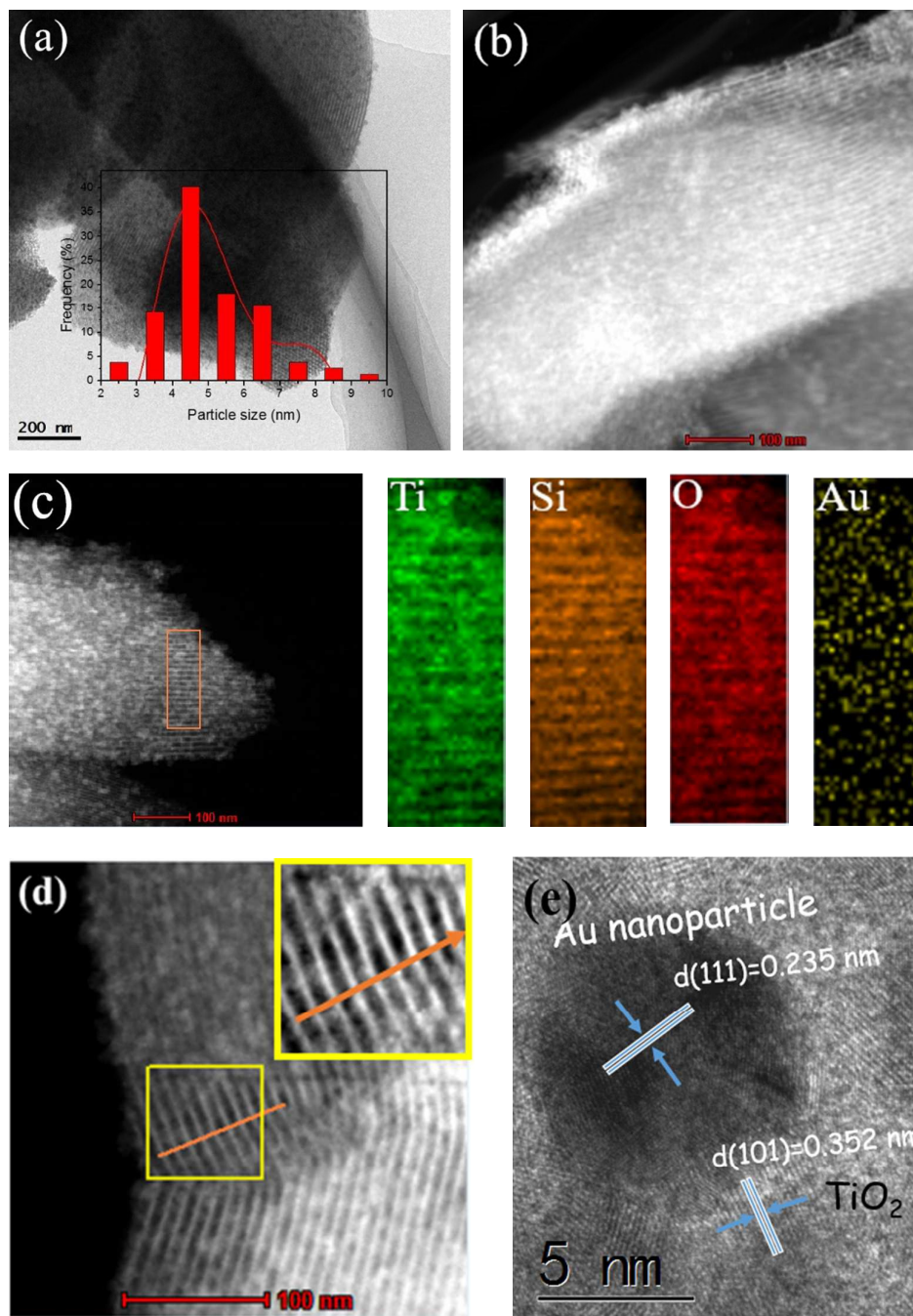
$$\text{Selectivity (\%)} = [C_{\text{aldehyde}}/(C_0 - C_{\text{alcohol}})] \times 100$$

where C_0 is the total amount of alcohols in the solution prior to illumination; C_{alcohol} is the amount of alcohols in the solution after illumination for 4h; C_{aldehyde} is the amount of aldehyde in the solution after illumination for 4h.

Results and discussion

Fig S1 shows the SEM image of the Au/TiO₂/SBA-15 composites thus prepared; short rod-like morphologies were observed, which retain the original shape of pristine SBA-15. Fig S2 (c-d) and Fig 1a show the TEM images of the as-prepared TiO₂/SBA-15 and Au₂/TiO₂/SBA-15 catalyst, respectively; highly ordered parallel nanotubular pores were observed along the [100] direction. The introduction of Au and titania in Au₂/TiO₂/SBA-15 did not substantially alter the regular ordered structure of the mesopores as compared with that in host SBA-15 (Fig S2 (a-b)). As can be observed from the TEM image, the Au NPs of the Au₂/TiO₂/SBA-15 catalyst were uniformly distributed in the channels of the SBA-15 support, with an average particle size of approximately 5.1 nm. For better observing the size distribution of the Au particles in these samples, the catalysts were further characterized by HAADF-STEM. The results (Fig 1b, d) show that the mean diameter of the Au NPs in the Au₂/TiO₂/SBA-15 sample is approximately 4.8 nm. Furthermore, Fig. 1(e) shows a high-resolution TEM (HRTEM) image of the Au NPs; lattice fringes with a d spacing of 0.235 nm were observed, corresponding to the Au(111) lattice planes.

This result indicates that the HAuCl_4 precursor is successfully converted to metallic Au nanoparticles, having a face-centered cubic structure, during reduction. In addition, another type of a lattice fringe was observed around the Au NPs, with a d spacing of approximately 0.352 nm, which can be indexed to the (101) plane of anatase TiO_2 . Moreover, the EDS elemental mapping of the STEM image shows that the Au, Ti, O, and Si elements are homogeneously distributed throughout the sample. Au was clearly observed in the mapping data, and the Au signals indicate that Au and TiO_2 NPs are in close contact with each other; this close contact and good incorporation between Au and TiO_2 , achieved by the microwave-assisted hydrothermal method, are believed to favor the transfer of photogenerated electrons through the interface between the Au NPs and TiO_2 , which in turn enhances charge separation and photocatalytic efficiency²⁶. The above deduction was further authenticated by the compositional line scanning profiles across the $\text{Au}_2/\text{TiO}_2/\text{SBA-15}$ catalyst (as shown in Fig 1(f)), obtained by HAADF-STEM-EDX, where Au and TiO_2 nanoparticles were uniformly distributed in the channels of the SBA-15 support. The further experiments were conducted with a series of specific amounts of Au (Au loading of 0, 0.5, 1, and 5): at a low Au loading of 0.5 and 1 wt% (Fig S2 (e-f)), small Au NPs with mean diameters of 3.7 and 4.4 nm were observed, indicating that the Au NPs are confined in the inner pores of mesoporous silica material rather than on the external surface. However, with further increase in the Au loading to 5 wt% (Fig S2 (g)), a small number of isolated Au NPs were observed, attributed to extensive particle agglomeration, with significant increase in the Au particle size to 8.3 nm. Moreover, the $\text{Au}_2/\text{TiO}_2/\text{SBA-15-PD}$ synthesized by photodeposition exhibited several gold aggregates on the surface of the support material (Fig S2 (h)). Hence, it can be concluded that the porous supports suppress the aggregation of Au nanoparticles, especially at low gold loading.



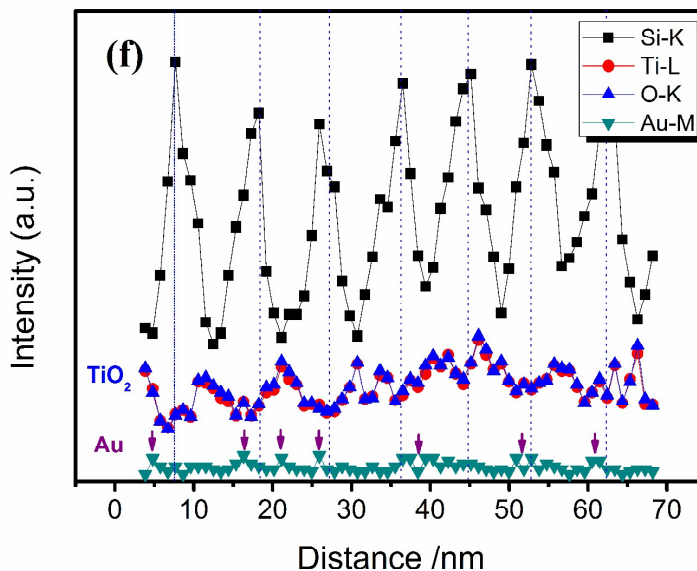
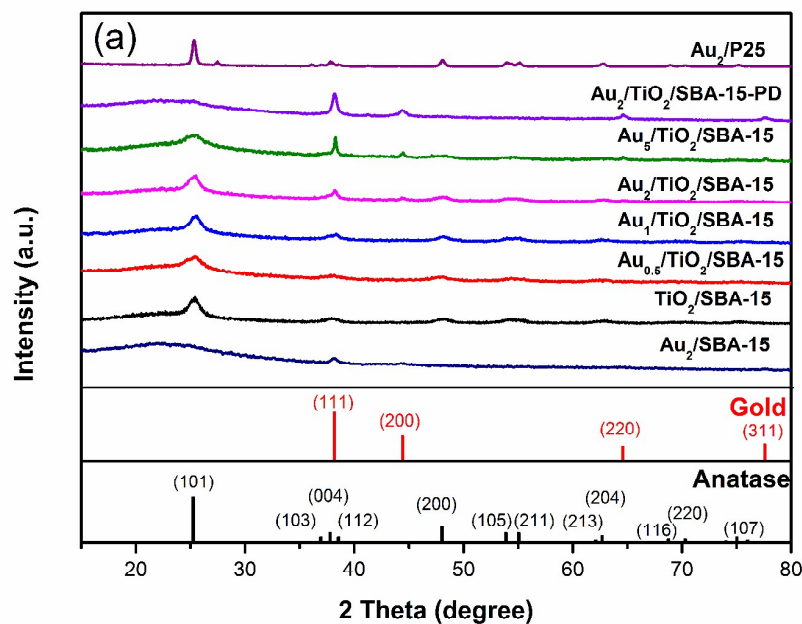


Fig 1 TEM image (a), HAADF-STEM image (b, d) and the STEM-EDS elemental mapping (c) of the $\text{Au}_2/\text{TiO}_2/\text{SBA-15}$ catalyst. HRTEM image (e) of interface between Au and TiO_2 and line-scanning profile (f) of $\text{Au}_2/\text{TiO}_2/\text{SBA-15}$ catalyst, which is indicated in the inset of (d).

Fig. 2 (a) shows the wide-angle XRD patterns of $\text{Au}_x/\text{TiO}_2/\text{SBA-15}$, $\text{Au}_2/\text{SBA-15}$, $\text{Au}_2/\text{TiO}_2/\text{SBA-15-PD}$ and $\text{Au}_2/\text{P25}$ composites. All samples exhibited characteristic broad peaks between 20° and 30° , attributed to amorphous silica in the SBA-15 framework²⁷. Titania-containing samples exhibited strong diffraction peaks at $2\theta = 25.5, 37.7, 48.1, 53.9, 55$ and 62.9° , attributed to (101), (004), (200), (105), (211) and (204) reflections respectively, these peaks indicate the presence of anatase TiO_2 and are in good agreement with JCPDS 21-1272. Diffraction peaks at $2\theta = 38.2, 44.6, 64.7$, and 77.5° , indexed to Au (111), (200), (220), and (311) reflections, respectively. The average crystalline sizes of $\text{Au}_x/\text{TiO}_2/\text{SBA-15}$ composites were in the range of 5.9 - 6.8 nm calculated according to the Scherrer formula (Table 1). This result is probably attributed to the generation of the titania seed crystals in the pore of SBA-15 and the limitation of the growth of titania crystals by the pore wall. On the other hand, by the introducing of Au into the $\text{TiO}_2/\text{SBA-15}$ sample, the $\text{Au}_x/\text{TiO}_2/\text{SBA-15}$ composites clearly exhibited diffraction peaks corresponding to Au: a broad, weak Au (111) diffraction peak indicated that the Au particles are well dispersed on the composites. However, the $\text{Au}_5/\text{TiO}_2/\text{SBA-15}$ sample clearly exhibited a diffraction peak of Au, suggesting that

the introduction of excessive Au in the sample results in the deposition of Au on the surface of the support material. Moreover, as compared to the $\text{Au}_2/\text{TiO}_2/\text{SBA-15}$ catalyst prepared by microwave-assisted alcohol reduction, the $\text{Au}_2/\text{TiO}_2/\text{SBA-15-PD}$ sample only exhibited clear Au diffraction peaks without titania, attributed to the aggregated of the Au NPs on the SBA-15 surface during the photo-deposition and blocking of most of the support channels, which is in accordance with the TEM results. Fig.2 (b) shows an integrated small-angle XRD pattern of pristine SBA-15, $\text{TiO}_2/\text{SBA-15}$, and the $\text{Au}_1/\text{TiO}_2/\text{SBA-15}$ composite. Three well-resolved peaks were observed, indexed to the 100, 110, and 200 planes of the 2D hexagonal mesostructure with $p6mm$ symmetry, respectively²⁸. As compared with that of pristine SBA-15, the primary diffraction peaks of $\text{TiO}_2/\text{SBA-15}$ and $\text{Au}/\text{TiO}_2/\text{SBA-15}$ shifted to higher angles, indicative of the marginal deposition of TiO_2 and Au in the mesopores.



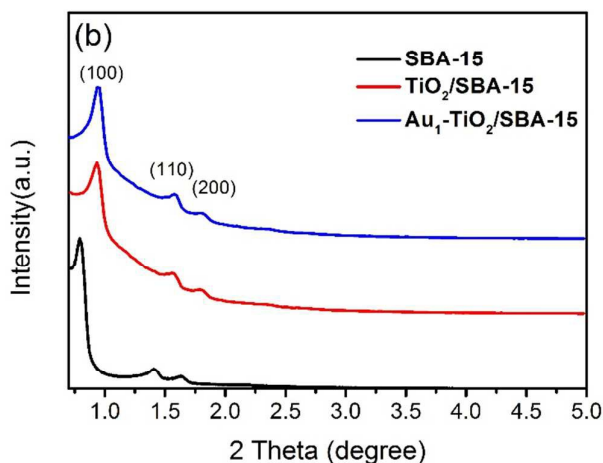


Fig 2 wide-(a) and small-angle (b) XRD patterns of $\text{TiO}_2/\text{SBA-15}$ and $\text{Au}_x/\text{TiO}_2/\text{SBA-15}$ samples

The structure parameters obtained from N_2 adsorption–desorption isotherms listed in Table 1. As can be observed, the Brunauer–Emmet–Teller (BET) surface area, pore volume, and average pore diameter decreased with the loading of titania, implying that most of the TiO_2 nanocrystals are loaded within the ordered channels of the support. Moreover, the pore distribution curves and isotherms of $\text{TiO}_2/\text{SBA-15}$ and $\text{Au}/\text{TiO}_2/\text{SBA-15}$ were almost the same, with barely any change in their pore diameters, indicating that the loading of small amount of Au NPs does not affect the mesoporous structure. Upon the introducing of a large amount of Au into $\text{TiO}_2/\text{SBA-15}$, the surface area and pore size of the catalyst significantly decreased, except for the $\text{Au}_2/\text{TiO}_2/\text{SBA-15-PD}$, which exhibited an average pore diameter greater than those of the other $\text{Au}_x/\text{TiO}_2/\text{SBA-15}$ samples. This result is attributed to the fact that the Au NPs aggregated on the surface can block most of the support channels, with a few channels remaining unfilled.

Table 1. Physicochemical properties of pristine SBA-15, $\text{TiO}_2/\text{SBA-15}$, $\text{Au}_x/\text{TiO}_2/\text{SBA-15}$ and $\text{Au}_2/\text{P25}$.

Samples	Au loading ^a (wt %)	Titania Size ^b nm	S_{BET} ^c m^2/g^{-1}	V_t ^d $\text{cm}^{-3}\text{g}^{-1}$	D_{BJH} ^e nm
SBA-15	0.00	n.a.	671.16	0.961	7.362
$\text{TiO}_2/\text{SBA-15}$	0.00	6.1	464.91	0.685	5.905

Au ₂ /SBA-15	1.98	n.a.	527.98	0.79	6.614
Au _{0.5} /TiO ₂ /SBA-15	0.29	5.9	466.83	0.687	5.882
Au ₁ /TiO ₂ /SBA-15	0.96	6.6	463.07	0.683	5.901
Au ₂ /TiO ₂ /SBA-15	1.87	6.5	459.81	0.685	5.764
Au ₅ /TiO ₂ /SBA-15	4.63	6.8	385.21	0.604	5.166
Au ₂ /TiO ₂ /SBA-15-PD	2.28	n.a.	408.62	0.574	5.982
Au ₂ /P25	2.08	24.9	43.09	0.193	17.47

^a Weight percentage of Au measured by EDS; ^b Crystal size of TiO₂ calculated according to the Scherrer formula; ^c S_{BET}, BET surface areas calculated by the adsorption branch of the N₂ isotherm; ^d V_t, total pore volume; ^e D_{BJH}, pore diameter determined by BJH model.

Fig. 3 shows the UV-vis absorption spectra of the as-prepared TiO₂/SBA-15 and Au_x/TiO₂/SBA-15 samples. Pure SBA-15 did not exhibit optical absorption²⁹. Hence, the absorption band edges observed between 300 and 400 nm in the titania-functionalized materials are associated with anatase. Furthermore, blue shifts were observed in the absorption spectra as compared to the spectrum position of bulk P25 TiO₂ powder. As had been previously reported for supported TiO₂, these blue shifts are attributed to quantum effects, which are observed for TiO₂ semiconductor having dimensions of less than 10 nm³⁰. Therefore, the shifts of the absorption spectra suggest that TiO₂ NPs were successfully loaded on porous silica in a dispersed state. Apparently, as compared to TiO₂/SBA-15, Au_x/TiO₂/SBA-15 exhibited a stronger absorption in the visible-light region, which was assigned to the characteristic LSPR peak of Au NPs. The surface plasmon absorption in the metal NPs arises from the collective oscillations of the free conduction band electrons that are enhanced by the incident electromagnetic radiation³¹. Moreover, the intensity of the LSPR band initially increased with increasing of Au loading amount up to 5.0%. It has been reported that the band position and intensity of the plasmon absorption strongly depend on the Au content, particle size of Au NPs, and the surrounding environment. Therefore, the increasing of SPR absorption peaks was probably ascribed to the increase in the particle sizes of Au for Au₅/TiO₂/SBA-15 and Au₂/TiO₂/SBA-15-PD, as partially evidenced by the TEM images shown in Fig. S2.

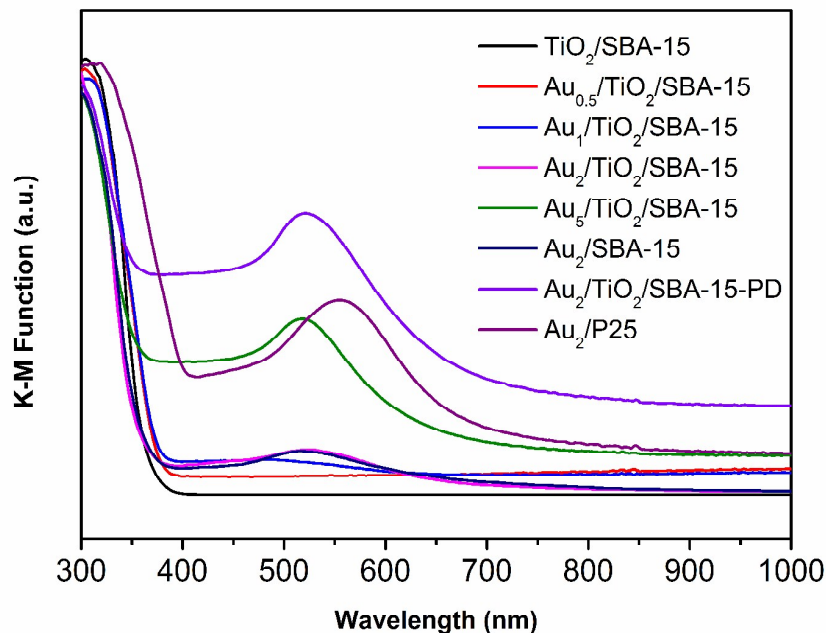


Fig 3. UV-vis diffuse reflectance spectra of as-prepared $\text{TiO}_2/\text{SBA-15}$, $\text{Au}_x/\text{TiO}_2/\text{SBA-15}$ and $\text{Au}_2/\text{P25}$.

XPS measurements were performed for $\text{Au}_2/\text{TiO}_2/\text{SBA-15}$ and $\text{Au}_2/\text{SBA-15}$ catalysts for obtaining further information about the chemical states of the Au species on the surface. As can be seen from Fig 4, $\text{Au}_2/\text{SBA-15}$ photocatalyst exhibited a doublet at 83.2 eV and 87.0 eV corresponding to Au $4f_{7/2}$ and Au $4f_{5/2}$ peaks, respectively, implying the presence of metallic Au^0 in the $\text{Au}_2/\text{SBA-15}$ sample^{32,33}. However, in the $\text{Au}_2/\text{TiO}_2/\text{SBA-15}$, Au 4f XPS peaks were significantly different, depending on the chemical states of Au³⁴. As shown in the deconvolution results, for $\text{Au}_2/\text{TiO}_2/\text{SBA-15}$, the Au species clearly existed in mixed oxidation states of Au^0 and Au^+ , which may be related to the electronic interaction between Au and TiO_2 . The catalytic activity of supported Au catalysts has been widely accepted to depend on the particle size of gold and the type and structure of oxide support³⁵⁻³⁸. For reducible supports such as TiO_2 , the presence of oxygen vacancies on the surface enables the adsorption and activation of O_2 , and the Au-oxide interface plays a crucial role in the oxidation of CO and alcohols^{3,39-41}. The oxygen activated by the oxide active sites generated partially by the interaction with Au is thought to react with a substrate (CO or alcohol) adsorbed on gold in close vicinity of the Au-oxide interface. On the other hand, for a non-reducible support such as SBA-15, oxygen adsorption

was suggested to occur on the defect sites of Au; thus, the photoactivity of this type of photocatalysts strongly depends on the Au particle size⁴²⁻⁴⁶.

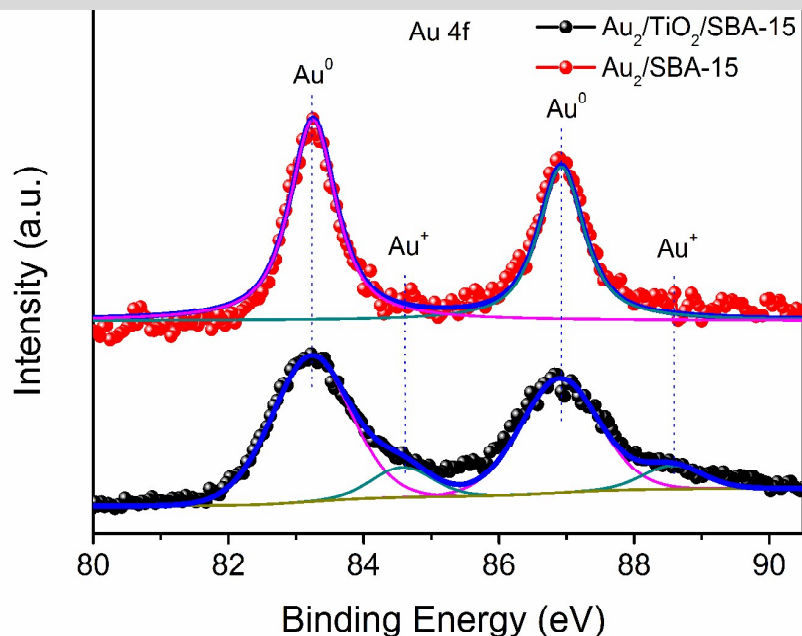


Fig 4. High-resolution XP spectra of Au 4f for the Au₂/TiO₂/SBA-15 and Au₂/SBA-15 samples.

For investigating the photocatalytic performance of Au_x/TiO₂/SBA-15 composites toward the oxidation of aromatic alcohols, the selective oxidation of benzyl alcohol was used as a model reaction⁴⁷⁻⁴⁹. First, the oxidation of benzyl alcohol was investigated without catalysts under visible-light irradiation. In this case, benzaldehyde was barely formed. Next, the reaction was performed by adding 50 mg of the catalyst under 1 atm O₂. The solution temperature was rigorously maintained at 303 K by a water-cooling system. Fig 5 summarizes the amounts of benzaldehyde formed after 4 h of reaction conducted in the dark or under visible-light irradiation (Xe lamp, 300 W, λ > 420 nm). Notably, benzaldehyde was selectively obtained in the presence of the catalyst, where the mass balance of benzyl alcohol and benzaldehyde was greater than 99%, and byproducts were not detected. In the dark, bare TiO₂ (TiO₂/SBA-15) cannot proceed the benzyl alcohol oxidation reaction, only 0.5% benzyl alcohol converted, while 27% benzyl alcohol was oxidized under visible light irradiation; this visible-light-driven activity is attributed to the ligand-to-metal charge transfer (LMCT) of the surface complex formed by the adsorption of

benzyl alcohol on the TiO_2 surface.^{50, 51} Subsequently, compared with P25, $\text{TiO}_2/\text{SBA-15}$ exhibited enhancement in activity, attributed to the decrease of the TiO_2 nanoparticle size with loading on the porous support, and small particles afforded high surface areas; hence, active site densities for heterogeneously catalyzed reactions.

Upon introducing Au into the $\text{TiO}_2/\text{SBA-15}$ sample, remarkable catalytic activity was observed for the oxidation of benzyl alcohol both in the dark and under visible-light irradiation. Among the supported gold catalysts, $\text{Au}_2/\text{TiO}_2/\text{SBA-15}$ exhibited the best performance. Under dark conditions, the $\text{Au}_2/\text{TiO}_2/\text{SBA-15}$ catalyst afforded 7.57 μmol of benzaldehyde, and light irradiation further enhanced the reaction: 45.54 μmol of benzaldehyde was produced, which is approximately 3.3 times greater than that obtained by the use of the $\text{TiO}_2/\text{SBA-15}$ catalyst; this result is consistent with previous studies in that Au-loaded TiO_2 markedly affected the catalytic activity with or without light irradiation. However, at a Au loading of 5 wt%, the photoassisted reaction resulted in a benzyl alcohol conversion less than that obtained with a lower gold loading. The statistic from the TEM survey (Fig S2) suggested that the mean Au particle diameter significantly increases in case of the excessive loading of the support material ($\text{TiO}_2/\text{SBA-15}$), resulting in a low active surface area, and hence low benzaldehyde yield. When $\text{Au}_2/\text{TiO}_2/\text{SBA-15-PD}$ was used as the catalyst, a yield of only 14.9 μmol of benzaldehyde was obtained. The decrease of yield under the same experiment conditions is attributed to the blocking of pores by several Au aggregates formed during photodeposition, resulting in the diffusion limitations of the reactants. Such a remarkable photoactivity enhancement of $\text{Au}_2/\text{TiO}_2/\text{SBA-15}$ could be attributed to the several factors. First of all, owing to the limit of host material SBA-15, the growth of TiO_2 particles were restricted by the walls of the channels, thus small and well dispersed TiO_2 nanoparticles were obtained. Small titania particles were in favor of the migration of charge carriers so that the recombination rate of them could be largely decreased. Secondly, the SBA-15 decorated by TiO_2 preserved a high surface area and possess a strong surface adsorption ability to alcohol molecules. Thus, the adsorbed alcohol molecules on catalytic sites can be supplied by the enriched adsorption sites near the TiO_2 particles, which can effectively decrease the diffusion limits of substrate and directly accelerate the reaction rate. And then, the intense LSPR-enhanced electromagnetic fields were generated on the surface of the Au nanoparticles, which significantly increased the yield of “hot electrons” at the interface. Thus, the localized electronic states

in the band gap of TiO_2 can be excited, and electrons can be transferred to the conduction band of TiO_2 . At last, the Schottky barrier at the Au– TiO_2 interface functions as a barrier for the transferred electrons, preventing them from traveling back to the Au nanoparticles and thus leading to an accumulation of these transferred electrons in the TiO_2 conduction band.

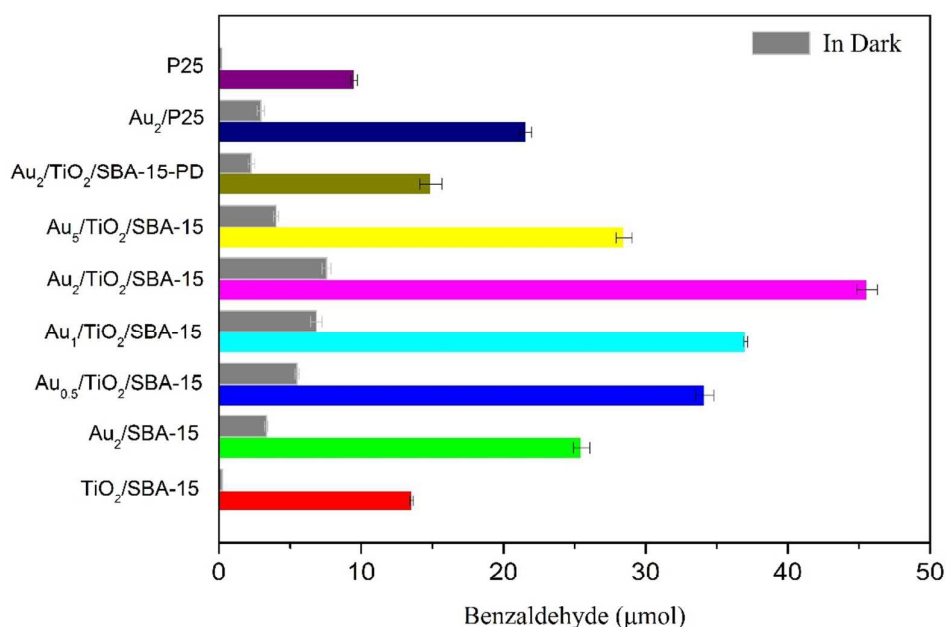


Fig 5. Amount of benzaldehyde formed during the oxidation of benzyl alcohol in the dark and under visible light irradiation ($\lambda > 420$ nm) over $\text{TiO}_2/\text{SBA-15}$, $\text{Au}_x/\text{TiO}_2/\text{SBA-15}$, $\text{Au}_2/\text{P25}$ and P25.

According to the previous research works, the porous silicate materials such as clays, zeolites and mesoporous silica are superior supports for accommodating photocatalysts nanoparticles, owing to their tunable pore sizes (2–50 nm), large surface areas, and fine connectivity of the pores facilitating the transfer of organic substrates^{43, 52}. In the present study, SBA-15, $\text{Au}_2/\text{TiO}_2/\text{SBA-15}$ and $\text{Au}_2/\text{P25}$ catalysts were selected as a model catalyst for FTIR measurement to determine the adsorption of benzyl alcohol on the mesoporous silica support. As the FTIR spectra (Fig 6) show that all samples exhibit a very broad band between 2750–3750 cm^{-1} , indicating the presence of hydrogen-bonded perturbed hydroxyl groups. As for the absorption spectrum of benzyl alcohol, the band at 1455 cm^{-1} is readily assigned to skeletal vibration of the aromatic ring. This absorption band can also be observed

on the SBA-15 and Au₂/TiO₂/SBA-15, which were treated by benzyl alcohol, indicating that molecular benzyl alcohol exists on these solid samples. On the contrary, the molecular benzyl alcohol was barely adsorbed on the catalyst of Au₂/P25. The result reflected that the adsorption of porous support (SBA-15) can effectively enrich the alcohol molecules in the tunnels, which played an identical role in photocatalytic processes.

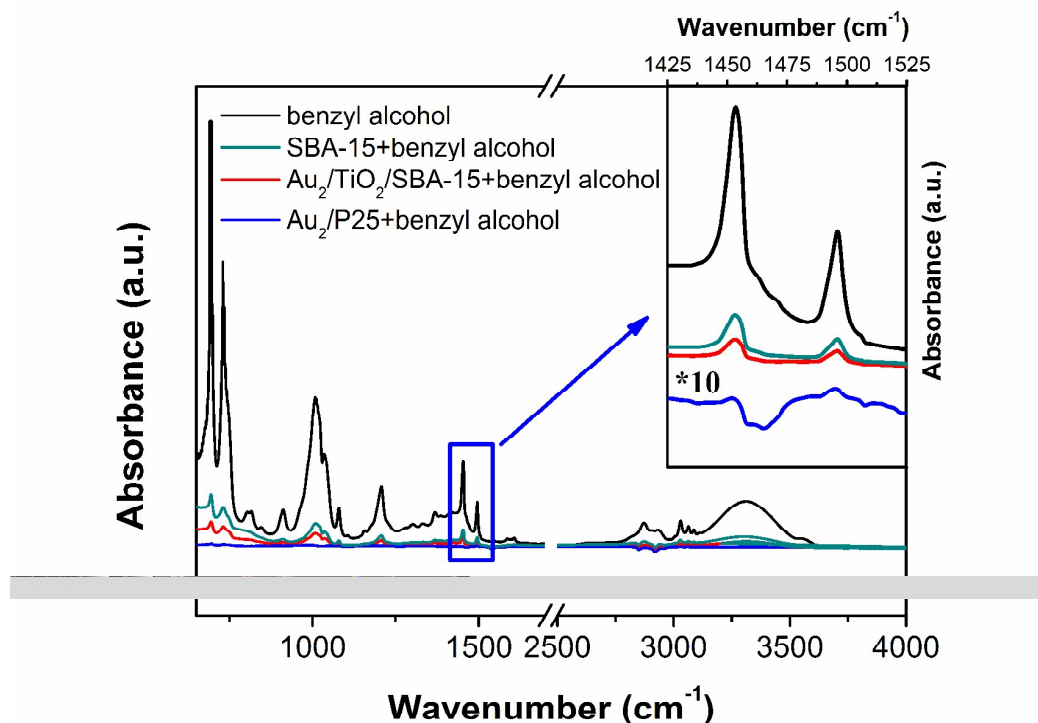


Figure 6. FTIR spectra of SBA-15, Au₂/TiO₂/SBA-15 and Au₂/P25 catalysts with adsorbed benzyl alcohol.

To better understand the enhancement mechanism of photocatalytic performance over Au₂/TiO₂/SBA-15 catalyst, the effects of wavelength range on the photoactivity were investigated. we used specific optical filter glasses (filter 1: 460 nm–800 nm, filter 2: 490 nm–800 nm, filter 3: 560 nm–800 nm, and filter 4: 620 nm–800 nm) for blocking light below cut-off wavelengths, and Fig 7 shows the results. Without any filter, light irradiation with wavelength in the complete 420 nm to 800 nm range resulted in a reaction yield of 91.08%. Using a filter transmitting wavelengths between 460 and 800 nm, the reaction yield decreased to 81.67%. On the other hand, by increasing the cut-off wavelength to 490 nm, the yield decreased to 75.84%, while increasing

the cut-off wavelength to 560 nm and then 620 nm resulted in yields decreasing to 37.06% and 20.23%, respectively. Under dark conditions, the thermal reaction yield of benzaldehyde was approximately 15.15%. As the reaction temperature was maintained constant (303K), the thermal effect contribution remained constant. Hence, we can estimate the contribution of the light in different wavelength ranges from the results acquired by irradiation with cut-off filters. Light irradiation in the wavelength range of 460 nm–620 nm resulted in the greatest enhancement in yield, accounting for 61.44% of the total light irradiation enhancement. The obtained reaction yields were also confirmed by irradiation using monochromatic light LEDs (Fig 8). When the reactor was illuminated with light of different wavelengths, such as blue (465–470 nm), yellow (485–490 nm), green (525–530 nm), and red (625–630 nm) with other experimental conditions constant, the trend of quantum yield was similar to that observed in the absorption spectrum. Given that the LSPR absorption of Au NPs occurs in the wavelength range between 460 nm and 600 nm, the Au₂/TiO₂/SBA-15 photocatalyst harvests visible light, resulting in a significant difference with respect to the enhancement of the reaction yield in photocatalysis.

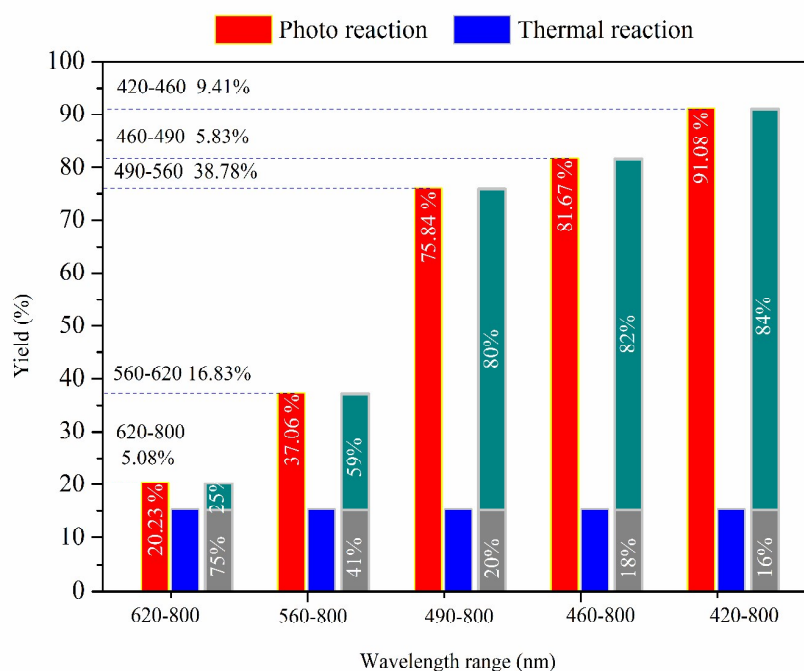


Fig 7. Dependence of yield and irradiation wavelength over the Au₂/TiO₂/SBA-15 catalyst for the selective oxidation of benzyl alcohol.

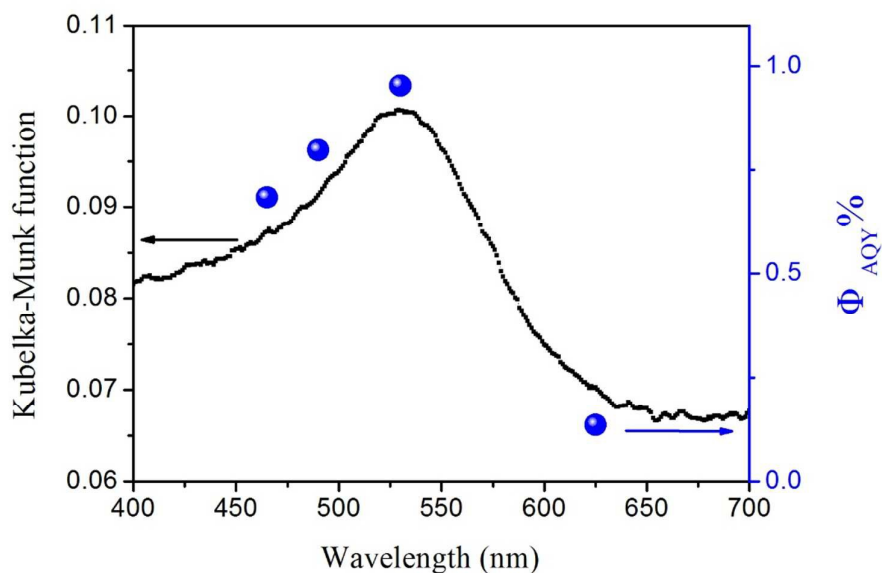


Fig 8. Diffuse-reflectance UV-vis spectra of the $\text{Au}_2/\text{TiO}_2/\text{SBA-15}$ catalyst and the quantum yield for the formation of benzaldehyde under LED lamp irradiation of different wavelengths, such as blue, green, yellow, and red light. The apparent quantum yield was calculated using the equation $\Phi_{AQY} = (Y_{vis} - Y_{dark}) / N \times 100\%$, where Y_{vis} and Y_{dark} denote the yield of benzaldehyde under light and dark conditions, respectively. N denotes the number of incident photons in the reaction vessel.

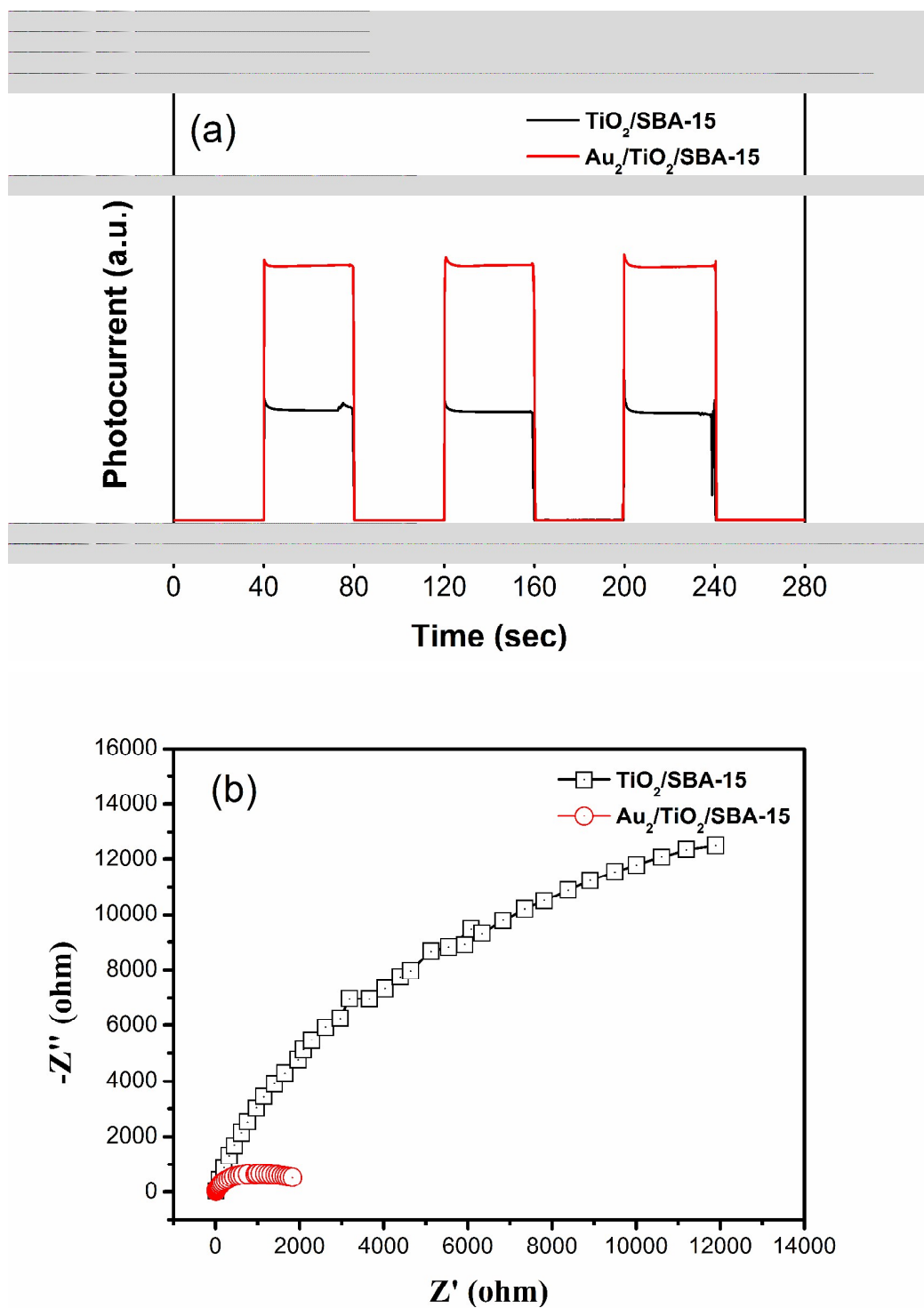


Fig 9. Photocurrent transient response (a) and electrochemical impedance spectroscopy Nyquist plots (b) of the sample electrodes of $\text{Au}_2/\text{TiO}_2/\text{SBA-15}$ and $\text{TiO}_2/\text{SBA-15}$ under visible light irradiation.

In order to determine the formation and transfer of photogenerated electrons from semiconductor

under light illumination, the photoelectrochemical characterizations were further authenticated. As shown in Fig 9(a), under visible light irradiation, the photocurrent intensity for Au₂/TiO₂/SBA-15 is much higher than that of TiO₂/SBA-15. The obvious increase in the transient photocurrent was mainly due to two aspects: (i) the Au NPs present can absorb visible light and generate more photoelectrons due to the LSPR effect. (ii) the formation of a Schottky junction at the Au-TiO₂ interface can separate the photoelectrons and holes, and thus increase the photocurrent. We subsequently utilized the electrochemical impedance spectra (EIS) experiments to investigate the electron generation and the charge transport characteristics of Au₂/TiO₂/SBA-15 and TiO₂/SBA-15. As can be seen from Fig 9(b), the Au₂/TiO₂/SBA-15 sample shows the smaller semicircle in the middle-frequency region, in comparison to the TiO₂/SBA-15, which indicates the more efficient interfacial electron transfer. Owing to the fact that the surface plasmon resonance effect of the Au NPs broadens the visible light response of the TiO₂, and the excellent electron transport properties hinders the fast recombination of photoelectron and hole pairs, such composite photocatalyst are largely beneficial for improving visible light photoactivity toward aerobic oxidation of alcohols.

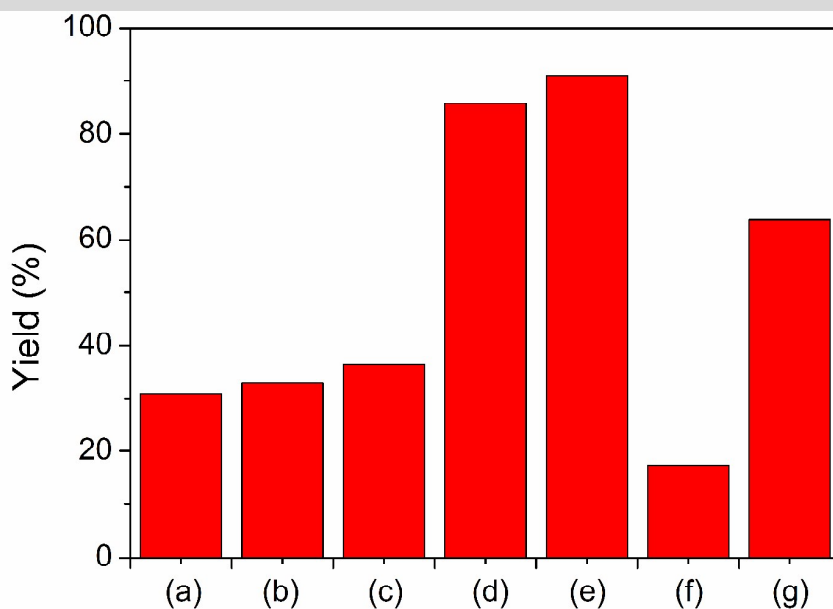


Fig 10. Controlled experiments using different radical scavengers (a) AgNO₃ for photogenerated electrons, (b) p-benzoquinone (BQ) for superoxide radicals; (c) ammonium oxalate (AO) for photogenerated holes; (d) tert-butyl alcohol (TBA) for hydroxyl radicals; (e) absence of radical

scavengers for the photocatalytic selective oxidation of benzyl alcohol over Au₂/TiO₂/SBA-15. React in the nitrogen atmosphere (f) and air atmosphere (g).

Herein, the underlying reaction mechanism involved for the photocatalytic oxidation of benzyl alcohol in water over Au₂/TiO₂/SBA-15 was investigated in detail. Previous studies have proven that molecular oxygen is the oxidizing agent for many photo-oxidation processes that are catalyzed by TiO₂. Moreover, this process is dominated by the adsorption of molecular oxygen on the surface of TiO₂ during the photocatalytic reaction. To better understand this process, we used different radical scavengers in controlled experiments to probe the reaction mechanism for the selective oxidation of benzyl alcohol over Au₂/TiO₂/SBA-15 under visible-light irradiation. As shown in Fig. 10, no significant change in the reaction process was observed when TBA was added to the reaction system to capture $\cdot\text{OH}$ radicals. However, an abrupt decrease in the conversion was observed upon the addition of either ammonium oxalate to capture photogenerated holes (h^+), AgNO₃ to capture photoelectrons (e^-), or benzoquinone to capture $\cdot\text{O}^{2-}$ radicals. Moreover, to investigate the role of molecular oxygen, the experiment was also conducted under nitrogen and air atmospheres. The trace conversion of benzyl alcohol in the nitrogen atmosphere was 17.3 %, but in the air atmosphere, a higher conversion was obtained (63.7%), but this conversion was still less than that in pure oxygen (91.1%). These results demonstrated that for aerobic oxidation of alcohols over Au₂/TiO₂/SBA-15 under visible light irradiation the positive holes, oxygen, or superoxide radicals play important roles instead of hydroxyl radicals.

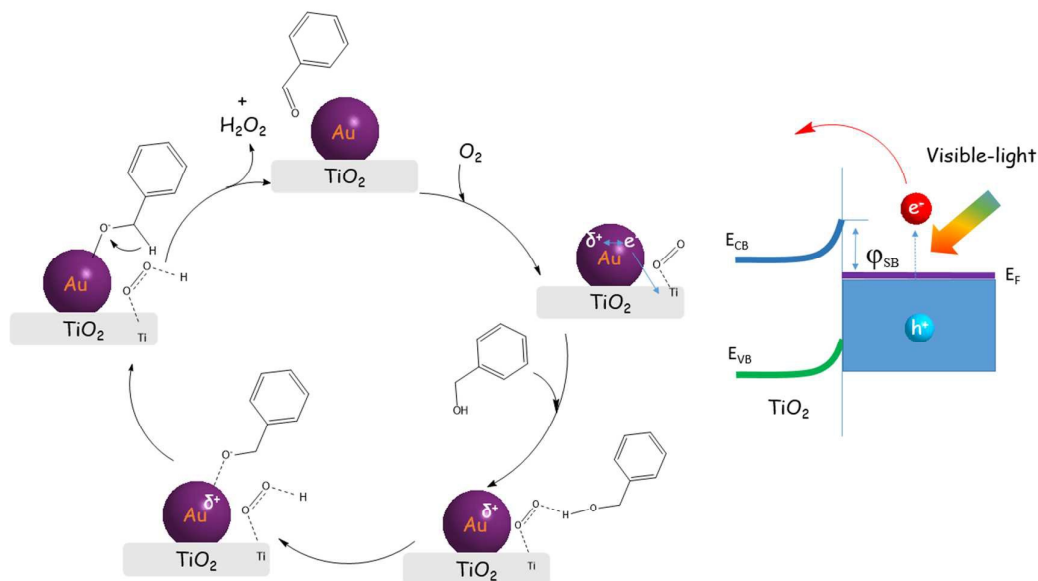


Fig 11. Expected reaction mechanism for the production of benzaldehyde from benzyl alcohol over $\text{Au}_2/\text{TiO}_2/\text{SBA-15}$ under visible-light irradiation. Fermi level (E_F), conduction (E_C) and valence (E_V) bands energy for Au, wide-bandgap semiconductor (TiO_2) of fabricated plasmonic nanostructure.

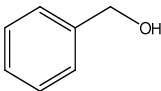
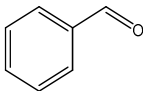
Considering the above results, the possible mechanism for the photocatalytic oxidation of aromatic alcohols over $\text{Au}_2/\text{TiO}_2/\text{SBA-15}$ was proposed, and Fig 11 shows the mechanism. Once Au and TiO_2 come into contact, a Schottky junction was formed at the interface between Au and TiO_2 , with the conduction and valence bands bending upward toward the TiO_2 interface⁵³. Under visible-light irradiation ($\lambda > 420$ nm), the incoming photons excited the LSPR of the Au NPs. Electrons oscillating collectively by LSPR excitation may result in intraband excitation, generating some hot electrons, the energies of which are greater than 1.0 eV with respect to the Au Fermi level. Then, the hot electrons with energies sufficiently high to overcome the Schottky barrier (ϕ_{SB}) are injected into the conduction band (E_C) of the neighboring TiO_2 . The hot electrons on the TiO_2 surface can be scavenged by molecular oxygen molecules, yielding an anion O-O^- species^{54,55}. These superoxide species can abstract the α -H atoms of benzyl alcohol, affording a transient alkoxide intermediate, which is considered to be the rate-determining step. Subsequently, the transient alkoxide intermediate undergoes the rapid transfer of hydride from C-H to positively charged Au, resulting in the elimination of β -H and affording the product. The proposed mechanism provides reasonable explanation for the enhancement of photooxidation induced by

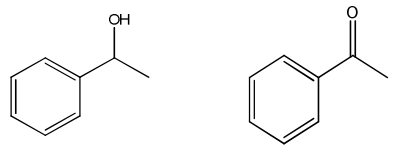
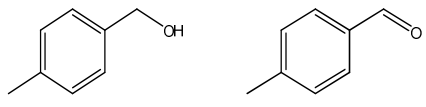
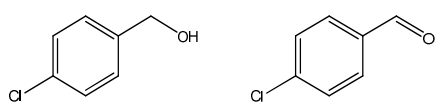
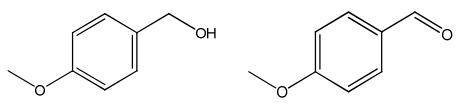
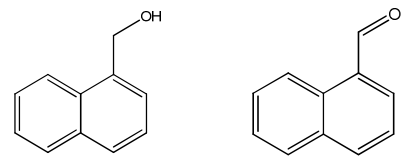
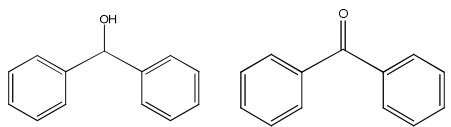
the LSPR effect under the visible-light irradiation of the Au₂/TiO₂/SBA-15 nanocomposite.

Initiated by the photoactivity of Au₂/TiO₂/SBA-15 for the selective oxidation of benzyl alcohol, we further investigated the photocatalytic oxidation of various aromatic alcohols over Au₂/TiO₂/SBA-15, TiO₂/SBA-15, and Au₂/P25, and Table 2 shows the results. As expected, Au₂/TiO₂/SBA-15 exhibited high activity for the oxidation of aromatic alcohols as well as good selectivity to carbonyl compounds, and the photocatalytic activity was several times greater than those obtained for reference TiO₂/SBA-15 and P25. Furthermore, the yields of different aromatic aldehydes or ketones were clearly different. The formation rate of para-substituted benzaldehyde over Au₂/TiO₂/SBA-15 decreased in the following order: -OCH₃ > -CH₃ > -H > -Cl, which is governed by the Hammett rule. This order indicates that the substitution of para-substituted benzylic alcohols with electron-releasing group such as -OCH₃ and -CH₃ increases the activity, while substitution with -Cl decreases the activity⁵¹. The above results suggested that the Au₂/TiO₂/SBA-15 composite is an excellent photocatalyst for the selective oxidation of aromatic alcohols to corresponding aldehydes.

It is important to note that the Au₂/TiO₂/SBA-15 nanocomposite exhibit good recyclability for the photocatalytic oxidation of benzyl alcohol. Fig S3 shows the reaction results. Using the fresh catalyst, the yield of benzaldehyde was 91.08%. After the first reaction cycles, the solid catalyst was recovered by centrifugation and dried for the next reaction cycle. For recycling, fresh benzyl alcohol and toluene were added, and the reaction conditions were the same as those employed in the first reaction cycle. From the second to the fourth reaction cycle, yields of 90.52%, 85.34%, and 84.3% were afforded. For the fifth reaction cycle, a conversion of greater than 79.15% was still achieved. By-products were not detected throughout these consecutive reaction cycles.

Table 2. Aerobic oxidation of aromatic alcohols over Au₂/TiO₂/SBA-15, TiO₂/SBA-15 and Au₂/P25 catalysts^a.

Entry	Substrate	Product	Catalyst	Yield ^b (%)	Selectivity ^c (%)	Reaction rate (μmol gcat ⁻¹ h ⁻¹)
1			Au ₂ /TiO ₂ /SBA-15	91.1	>99	227.4
			TiO ₂ /SBA-15	27.1	>99	67.68

			Au ₂ /P25	43.1	>99	107.63
2			Au ₂ /TiO ₂ /SBA-15	56.8	97.1	137.8
			TiO ₂ /SBA-15	12.7	84.6	26.8
			Au ₂ /P25	19.8	89.8	44.45
3			Au ₂ /TiO ₂ /SBA-15	93.9	>99	234.5
			TiO ₂ /SBA-15	39.9	83.1	82.89
			Au ₂ /P25	64.5	91.7	147.87
4			Au ₂ /TiO ₂ /SBA-15	75.1	80.4	150.9
			TiO ₂ /SBA-15	18.7	54.1	25.29
			Au ₂ /P25	30.0	71.2	53.4
5			Au ₂ /TiO ₂ /SBA-15	99.9	>99	250.0
			TiO ₂ /SBA-15	54.4	82.5	112.2
			Au ₂ /P25	89.1	96.1	214.06
6			Au ₂ /TiO ₂ /SBA-15	87.3	87.6	191.2
			TiO ₂ /SBA-15	41.2	55.5	57.16
			Au ₂ /P25	70.6	73.8	130.26
7			Au ₂ /TiO ₂ /SBA-15	77.6	91.5	177.5
			TiO ₂ /SBA-15	23.5	60.1	35.31
			Au ₂ /P25	44.6	74.2	82.73

^a Reaction conditions: toluene (5 mL), alcohol (50 μmol), catalyst (50 mg), O₂ (1 atm).

^b Aromatic aldehyde yield at time-on-stream of 4 h.

^c selective of aldehyde or ketone at time-on-stream of 4 h.

Conclusion

In summary, a series of gold-promoted TiO₂/SBA-15 catalysts were prepared by a facile, rapid microwave-assisted alcohol reduction method, exhibiting visible-light response for the photocatalytic selective oxidation of alcohols. Comprehensive experimental measurements were conducted using these catalysts for correlating the catalytic activity with the corresponding loading amount and size of Au NPs. As compared with that of benchmark P25, the surface area of

anatase TiO₂ nanoparticles and absorption ability dramatically increased through interaction with these porous supports as the key parameter affecting photocatalytic activity. In addition, small domains of monodisperse mesoporous silica resulted in the homogeneous deposition of Au NPs inside the pores of the support, resulting in small Au NPs with a mean diameter of 4.8 nm for a Au loading at 2 wt%. And the gold nanoparticles deposited onto TiO₂ can greatly improve the photocatalytic performance of alcohol oxidation. This enhancement effect may be attributed to the increase in the formation rate of electron-hole pairs induced by LSPR of Au NPs and higher efficiency of electron transfer due to the Schottky barrier at the Au-TiO₂ interface. The simple strategy and materials developed here dramatically improved photocatalytic activity and can also be applied to other traditional catalytic reactions.

Acknowledgements

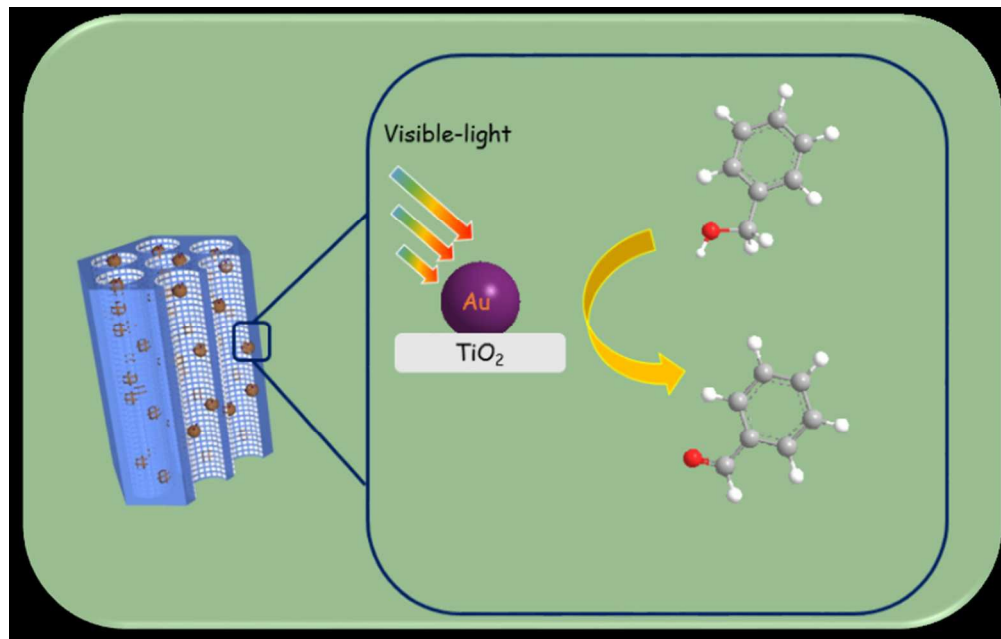
This work was supported by International Joint Research Projects in the Science & Technology Pillar Program of Tianjin, China (13RCGFSF14300), Research Projects in the Science & Technology Pillar Program of Tianjin, China (14TXGCCX00012), Research Projects in the Science & Technology Pillar Program of Tianjin, China (15JCTPJC63300), Research Projects in the Science & Technology Program of Jinnan District Tianjin, China (2015JNKW0005) and the Ph.D. Candidate Research Innovation Fund of Nankai University.

References

1. T. Mallat and A. Baiker, *Chem. Rev.*, 2004, 104, 3037-3058.
2. D. I. Enache, J. K. Edwards, P. Landon, B. Solsona-Espriu, A. F. Carley, A. A. Herzing, M. Watanabe, C. J. Kiely, D. W. Knight and G. J. Hutchings, *Science*, 2006, 311, 362-365.
3. A. Abad, P. Concepción, A. Corma and H. García, *Angew. Chem. Int. Ed.*, 2005, 44, 4066-4069.
4. C. Y. Ma, B. J. Dou, J. J. Li, J. Cheng, Q. Hu, Z. P. Hao and S. Z. Qiao, *Appl. Catal. B Environ.*, 2009, 92, 202-208.
5. A. Tanaka, K. Hashimoto and H. Kominami, *J. Am. Chem. Soc.*, 2012, 134, 14526-14533.
6. G. J. Ten Brink, I. W. C. E. Arends and R. A. Sheldon, *Science*, 2000, 287, 1636-1639.
7. F. M. Menger and C. Lee, *Tetrahedron Letters*, 1981, 22, 1655-1656.
8. V. Augugliaro, G. Camera-Roda, V. Loddo, G. Palmisano, L. Palmisano, J. Soria and S. Yurdakal, *J. Phys. Chem. Lett.*, 2015, 6, 1968-1981.
9. J. C. Colmenares and R. Luque, *Chem. Soc. Rev.*, 2014, 43, 765-778.

10. N. Zhang, Y. Zhang, X. Pan, X. Fu, S. Liu and Y. J. Xu, *J. Phys. Chem. C*, 2011, 115, 23501-23511.
11. S. Yurdakal, G. Palmisano, V. Loddo, V. Augugliaro and L. Palmisano, *J. Am. Chem. Soc.*, 2008, 130, 1568-1569.
12. M. Zhang, C. Chen, W. Ma and J. Zhao, *Angew. Chem. Int. Ed.*, 2008, 47, 9730-9733.
13. M. Zhang, Q. Wang, C. Chen, L. Zang, W. Ma and J. Zhao, *Angew. Chem. Int. Ed.*, 2009, 48, 6081-6084.
14. S. Sarina, H. Zhu, E. Jaatinen, Q. Xiao, H. Liu, J. Jia, C. Chen and J. Zhao, *Journal of the American Chemical Society*, 2013, 135, 5793-5801.
15. Y. Chen, W. Li, J. Wang, Y. Gan, L. Liu and M. Ju, *Applied Catalysis B: Environmental*, 2016, 191, 94-105.
16. X. Pan and Y. J. Xu, *ACS Appl. Mater. Interfaces*, 2014, 6, 1879-1886.
17. X. Dai, M. Xie, S. Meng, X. Fu and S. Chen, *Appl. Catal. B Environ.*, 2014, 158-159, 382-390.
18. C. Wang and D. Astruc, *Chem. Soc. Rev.*, 2014, 43, 7188-7216.
19. S. Linic, P. Christopher and D. B. Ingram, *Nature Materials*, 2011, 10, 911-921.
20. K. Awazu, M. Fujimaki, C. Rockstuhl, J. Tominaga, H. Murakami, Y. Ohki, N. Yoshida and T. Watanabe, *Journal of the American Chemical Society*, 2008, 130, 1676-1680.
21. P. Zhang, T. D. Wang and J. Gong, *Adv Mater.*, 2015, 27, 5328-5342.
22. D. Tsukamoto, Y. Shiraishi, Y. Sugano, S. Ichikawa, S. Tanaka and T. Hirai, *J. Am. Chem. Soc.*, 2012, 134, 6309-6315.
23. S. Schünemann, G. Dodekatos and H. Tüysüz, *Chem. Mater.*, 2015, 27, 7743-7750.
24. K. Qian, B. C. Sweeny, A. C. Johnston-Peck, W. Niu, J. O. Graham, J. S. Duchene, J. Qiu, Y. C. Wang, M. H. Engelhard, D. Su, E. A. Stach and W. D. Wei, *Journal of the American Chemical Society*, 2014, 136, 9842-9845.
25. Y. Chen, J. Wang, W. Li and M. Ju, *Mater Lett*, 2015, 159, 131-134.
26. D. Ding, K. Liu, S. He, C. Gao and Y. Yin, *Nano Lett.*, 2014, 14, 6731-6736.
27. X. Li, W. Zheng, H. Pan, Y. Yu, L. Chen and P. Wu, *J. Catal.*, 2013, 300, 9-19.
28. X. F. Qian, T. Kamegawa, K. Mori, H. X. Li and H. Yamashita, *J. Phys. Chem. C*, 2013, 117, 19544-19551.
29. A. Corma and H. Garcia, *Chem. Commun.*, 2004, DOI: 10.1039/B400147H, 1443-1459.
30. M. Anpo and J. M. Thomas, *Chem. Commun.*, 2006, DOI: 10.1039/b606738g, 3273-3278.
31. M. Murdoch, G. I. N. Waterhouse, M. A. Nadeem, J. B. Metson, M. A. Keane, R. F. Howe, J. Llorca and H. Idriss, *Nat. Chem.*, 2011, 3, 489-492.
32. S. Zhu, S. Liang, Q. Gu, L. Xie, J. Wang, Z. Ding and P. Liu, *Applied Catalysis B: Environmental*, 2012, 119-120, 146-155.
33. N. Kruse and S. Chenakin, *Appl. Catal. A Gen.*, 2011, 391, 367-376.
34. Y. Wang, J. Yu, W. Xiao and Q. Li, *J. Mater. Chem. A*, 2014, 2, 3847-3855.
35. T. Wang, X. Yuan, S. Li, L. Zeng and J. Gong, *Nanoscale*, 2015, 7, 7593-7602.
36. M. P. Casaletto, A. Longo, A. M. Venezia, A. Martorana and A. Prestianni, *Appl. Catal. A Gen.*, 2006, 302, 309-316.
37. M. Han, X. Wang, Y. Shen, C. Tang, G. Li and R. L. Smith Jr, *J. Phys. Chem. C*, 2010, 114, 793-798.
38. F. Ying, S. Wang, C. T. Au and S. Y. Lai, *Gold Bulletin*, 2010, 43, 241-251.

39. M. Farnesicamellone, J. Zhao, L. Jin, Y. Wang, M. Muhler and D. Marx, *Angew. Chem. Int. Ed.*, 2013, 52, 5780-5784.
40. J. Wang, B. Li, T. Gu, T. Ming, J. Wang, P. Wang and J. C. Yu, *ACS Nano*, 2014, 8, 8152-8162.
41. B. Mei, C. Wiktor, S. Turner, A. Pougin, G. Van Tendeloo, R. A. Fischer, M. Muhler and J. Strunk, *ACS Catal.*, 2013, 3, 3041-3049.
42. C. J. Liu, Y. Zhao, Y. Li, D. S. Zhang, Z. Chang and X. H. Bu, *ACS Sustainable Chem. Eng.*, 2014, 2, 3-13.
43. X. Zhang, X. Ke and H. Zhu, *Chemistry - A European Journal*, 2012, 18, 8048-8056.
44. X. Yang, C. Huang, Z. Fu, H. Song, S. Liao, Y. Su, L. Du and X. Li, *Appl. Catal. B Environ.*, 2013, 140-141, 419-425.
45. L. Guzzi, G. Petö, A. Beck, K. Frey, O. Geszti, G. Molnár and C. Daróczy, *J. Am. Chem. Soc.*, 2003, 125, 4332-4337.
46. H. Tsunoyama, H. Sakurai, Y. Negishi and T. Tsukuda, *J. Am. Chem. Soc.*, 2005, 127, 9374-9375.
47. S. Verma, R. B. N. Baig, M. N. Nadagouda and R. S. Varma, *ACS Sustainable Chemistry & Engineering*, 2015, DOI: 10.1021/acssuschemeng.5b01163.
48. Y. Sugano, Y. Shiraishi, D. Tsukamoto, S. Ichikawa, S. Tanaka and T. Hirai, *Angewandte Chemie - International Edition*, 2013, 52, 5295-5299.
49. T. Jiang, C. Jia, L. Zhang, S. He, Y. Sang, H. Li, Y. Li, X. Xu and H. Liu, *Nanoscale*, 2015, 7, 209-217.
50. S. Higashimoto, N. Kitao, N. Yoshida, T. Sakura, M. Azuma, H. Ohue and Y. Sakata, *J. Catal.*, 2009, 266, 279-285.
51. S. Higashimoto, N. Suetsugu, M. Azuma, H. Ohue and Y. Sakata, *Journal of Catalysis*, 2010, 274, 76-83.
52. K. Mori, P. Verma, R. Hayashi, K. Fuku and H. Yamashita, *Chemistry - A European Journal*, 2015, 21, 11885-11893.
53. C. Clavero, *Nature Photonics*, 2014, 8, 95-103.
54. P. Christopher, H. Xin, A. Marimuthu and S. Linic, *Nat. Mater.*, 2012, 11, 1044-1050.
55. P. Christopher, H. Xin and S. Linic, *Nat. Chem.*, 2011, 3, 467-472.



229x146mm (96 x 96 DPI)